JGR Space Physics

RESEARCH ARTICLE
10.1029/2022JA030491

Key Points:

- Before Ultra-Low Frequency (ULF) waves begin to grow the magnetotail stretches, closer to Earth this occurs later: <10 min before the ULF wave excitation
- Peak ULF wave power is associated the fast planetward and azimuthal flows (median 80 − 100 kms^{-1})
- The local energy density is found to increase during the ULF wave growth, likely showing the transport of energy into this region

Correspondence to:

A. W. Smith,
andy.w.smith@ucl.ac.uk

Citation:

Smith, A. W., Rae, I. J., Forsyth, C., Watt, C. E. J., & Murphy, K. R. (2023). Statistical characterization of the dynamic near-Earth plasma sheet relative to Ultra-Low Frequency (ULF) wave growth at substorm onset. *Journal of Geophysical Research: Space Physics*, *128*, e2022JA030491. https://doi.org/10.1029/2022JA030491

Received 23 MAR 2022
Accepted 3 JAN 2023

Statistical Characterization of the Dynamic Near-Earth Plasma Sheet Relative to Ultra-Low Frequency (ULF) Wave Growth at Substorm Onset

A. W. Smith[1,2], I. J. Rae[2], C. Forsyth[1], C. E. J. Watt[2], and K. R. Murphy[2]

[1]Mullard Space Science Laboratory, University College London, Dorking, UK, [2]Department of Mathematics, Physics and Electrical Engineering, Northumbria University, Newcastle upon Tyne, UK

Abstract Magnetospheric substorms are a complex phenomenon. During the initial stages of a substorm a variety of important processes occur in near-Earth space within a span of several minutes. The relative timing and links between these processes are critical to understanding how, where and when substorms may occur. One of the first observed signatures at substorm onset is the exponential increase in ULF (Ultra-Low Frequency) wave power in the near-Earth magnetotail (e.g., $-7.5 \leq X_{GSM} \leq -12.5\ R_E$). We use the Time History of Events and Macroscale Interactions during Substorms spacecraft to examine the conditions in the magnetotail plasma sheet before, during and after local ULF wave growth. Prior to the ULF wave growth, the magnetotail stretches with convectional flows dominating. We then find strong earthward and azimuthal flows that peak at a similar time to the peak ULF wave power. These flows are found to be faster in the mid-tail ($-10 \leq X_{GSM} \leq -12.5\ R_E$) than the near-tail ($-7.5 \leq X_{GSM} \leq -10\ R_E$). Examining the local plasma energy density (magnetic, thermal and kinetic), we find no statistical decrease that could explain the exponentially growing ULF waves, in fact the local energy density is found to increase. This suggests that there may be an injection of energy from elsewhere in the magnetotail. Following the peak ULF wave power the tail is seen to dipolarize, and the local energy density is enhanced.

Plain Language Summary Substorm onset is an explosive process most often linked with the sudden, dramatic brightening of the aurora. Often within the brightening auroral there are regular, periodic bright structures known as auroral beads. While they are nearly ubiquitous, the origin of these auroral beads is poorly understood. However, they have been linked to local, fast growing fluctuations in the magnetic field that can be observed at the same time and at the same location as the beads. These fluctuations have been found to be generated in the plasma environment of near-Earth space before traveling to the ground. Here, we investigate what is happening in the near-Earth source region as these magnetic fluctuations are growing. We find that the magnetic fluctuations grow during highly dynamic conditions in the magnetotail, with fast plasma flows that peak at the same time as the most intense magnetic fluctuations. We investigate, testing whether there is a local source of energy that can explain the growing magnetic perturbations, instead finding that there may be an external source of energy.

1. Introduction

Magnetospheric substorms are cycles of energy storage and release, driven through the interaction of the Earth's magnetic field with the Interplanetary Magnetic Field (IMF) that is associated with the solar wind. In the initial growth phase, reconnection between the IMF and the Earth's magnetic field "opens" the magnetospheric field, such that one end is connected to the Earth and the other is connected to the Sun. The open field convects with the solar wind flow across the polar regions of the Earth, before residing in the magnetotail lobes on the nightside of the planet (McPherron, 1970). This process accumulates energy in the magnetotail, causing changes in the field geometry and plasma properties (e.g., Runov et al., 2021 and references therein) before the start of the next phase: the expansion phase (Akasofu, 1964).

The start of the expansion phase is sometimes known as substorm onset. During this phase, a series of processes occur on the nightside of the Earth, with consequences that can be observed on the ground (e.g., Murphy et al., 2022). In the near-Earth magnetotail (~10 R_E from the Earth, 1 R_E = 6,371 km), the cross-tail current is diverted into the ionosphere in a newly formed current system known as the Substorm Current Wedge (SCW; e.g., Murphy et al., 2013; Kepko et al., 2015, and references therein). Further from the planet (~20 R_E from

the Earth), magnetic reconnection produces strong planetward flows known as Bursty Bulk Flows (BBFs; Angelopoulos et al., 1992; Baumjohann et al., 1990; Hones et al., 1984) as well as complex magnetic structures (Eastwood & Kiehas, 2015; Slavin et al., 1989, 1995; and references therein). The reconnection process closes "open" magnetic field, such that the field is now once again connected at both ends to the Earth (Hones et al., 1984). Activations in both these regions have been associated with expansion phase onset, but how the physical processes at each location are connected remains unclear to this day (e.g., Angelopoulos et al., 2008; Donovan et al., 2008; Murphy et al., 2014; Rae, Mann, Angelopoulos, et al., 2009; Runov et al., 2008; Sergeev et al., 2008, 2012).

On the ground, the expansion phase can be seen to begin with the brightening of an auroral arc (Akasofu, 1977). Within the brightening arc azimuthal structure, known as auroral beads, can often be observed (Henderson, 1994; Kalmoni et al., 2017; Rae, Mann, Murphy, et al., 2009). Such structure can sometimes be seen for ∼10–20 min before auroral breakup (Uritsky et al., 2009). Auroral beads have spatial scales of between ∼30 and ∼150 km (Chang & Cheng, 2015; Friedrich et al., 2001; Sakaguchi et al., 2009), while detailed Fourier analysis of the brightening arc has demonstrated that the brightness of these unstable spatial scales grow exponentially (Kalmoni et al., 2015; Rae et al., 2010). Further high cadence analytical studies of the structuring has revealed that it is consistent with generation by shear Alfén waves of short perpendicular scale (Kalmoni et al., 2018), propagating into the ionosphere from near-Earth space (Smith, Rae, Forsyth, Watt, Murphy, & Mann, 2020). Moreover, auroral beads have been found to be nearly ubiquitous at substorm onset (Kalmoni et al., 2017), suggesting that the processes responsible may be related to key physics at the start of the expansion phase.

Providing a further clue as to their origin, auroral beads have been linked to coincident and exponentially growing Ultra-Low Frequency (ULF) wave power (Rae et al., 2012; Smith, Rae, Forsyth, Watt, & Murphy, 2020; Voronkov et al., 2003). While individual wavepackets may present with a dominant ULF period, the period is found to vary between events such that the statistical power spectrum can be best represented by a power law (Murphy et al., 2011). Nonetheless, the dominant wave periods have been found to be within the approximate period range 24–96s (Rae et al., 2011, 2017), termed the Pi1-2 band. The exponentially growing wave power has also been found to spread from an epicenter (Milling et al., 2008; Smith, Rae, Forsyth, Watt, Murphy, & Mann, 2020), a location that is also associated with the first global auroral brightening (Murphy et al., 2009), further highlighting the significance of the location at which the processes are occurring.

Mapping the ULF waves and associated auroral beads back into the magnetosphere would suggest a source region in the near-Earth magnetotail, between 8 and 12 R_E from the Earth (Donovan et al., 2008; Kalmoni et al., 2018), in a similar region to that in which the SCW has been inferred to form (Kepko et al., 2015 and references therein). Such a source region is also supported by the observations of conjugate auroral bead structures in both hemispheres (Motoba et al., 2012), and the observations that the auroral bead properties may be related to the configuration of the plasma sheet (Nishimura et al., 2016). Recently, Smith, Rae, Forsyth, Watt, and Murphy (2020) surveyed this approximate region at substorm onset, finding consistent observations of exponential ULF wave growth that on average lead the ground by 1–2 min. Further, Smith, Rae, Forsyth, Watt, Murphy, and Mann (2020) compared the ground and space-based ULF wave observations as a function of wave period, providing further evidence that the propagation of these ULF waves to the ground is consistent with the properties of shear Alfvén waves.

However, the precise phenomenon responsible is not yet clear. There have been several candidate plasma instabilities proposed to generate such ULF waves in the near-Earth magnetotail (A. Lui, 2004). These include but are not limited to: the cross-field current instability (A. T. Y. Lui et al., 1991); ballooning instabilities such as the shear flow (Voronkov et al., 1997), pressure anisotropy (Oberhagemann & Mann, 2020) and kinetic variants (Cheng, 2004; Panov et al., 2012); the current-driven Alfvénic instability (Perraut et al., 2000); or other non-magnetohydrodynamic (non-MHD) processes (Haerendel & Frey, 2021; Nishimura et al., 2022). However, ULF waves in the period band of interest may also be generated by convective flows in the magnetotail (e.g., Horvath & Lovell, 2019; Keiling & Takahashi, 2011; Kim et al., 2007; Ream et al., 2015). With this work, we provide insight and observational constraints on the processes active close to the source region of the ULF wave onset. We examine the conditions before, during and after the ULF wave activations, potentially related to an instability in the near-Earth magnetotail.

2. Data and Method

In this work, we utilize data from the Time History of Events and Macroscale Interactions during Substorms (THEMIS) mission (Angelopoulos, 2008). Three THEMIS spacecraft (THEMIS A, D, and E) surveyed the near-Earth plasma sheet in the first half of 2009 with a separation of only around 1 R_E. We use data from the fluxgate magnetometers (Auster et al., 2009), and moments calculated from the combined Electrostatic Analyzer and Solid State Telescope observations (McFadden et al., 2009), both at 4 Hz. We predominantly use data in the Geocentric-Solar-Magnetospheric (GSM) coordinate system; where the X-axis outlines the Earth-Sun line, the Z is aligned with the projection of the Earth's dipole axis into the plane perpendicular to X, while the Y axis completes the right handed system.

We limit our investigation to those intervals of time around expansion phase onsets. To do this, we use the Substorm Onsets and Phases from Indices of the Electrojet (SOPHIE) technique (Forsyth et al., 2015), selecting those onsets above the 90th percentile (Expansion Percentile Threshold, EPT = 90). While the 75th percentile (EPT = 75) has been shown to give good agreement with independent auroral-based onset catalogs, we presume that the use of the higher percentile limit will minimize the inclusion of large pseudo-breakups. As we wish to examine the changes in the near-Earth magnetotail before onset, we remove any onsets that are preceded by less than 90 min of quiet, that is, compound substorm events.

We use the period of time from 15th January to 30 April 2009, when the THEMIS spacecraft regularly passed through the near-Earth plasma sheet. This period of time was previously studied by Smith, Rae, Forsyth, Watt, and Murphy (2020), who compared the ULF waves observed by the THEMIS spacecraft at substorm onset with those recorded at conjugate locations on the ground. A total of 506 expansion phase onsets (using EPT = 90) were observed in this time period, of which 335 were determined to be "isolated" according to our 90 min criterion. We then down-selected based on spacecraft location, requiring that at least one of the THEMIS spacecraft was approximately within the near-Earth plasma sheet:

- $-12.5 \leq X_{\mathrm{GSM}} \leq -7.5\ R_E$
- $-5 \leq Y_{\mathrm{GSM}} \leq 5\ R_E$
- $-5 \leq Z_{\mathrm{GSM}} \leq 5\ R_E$

This limits our study to a maximum of 471 intervals of spacecraft observations within the appropriate region during substorm onset. We then calculated the wave power in the magnetic field observations using a bandpass filter for periods between 10 and 100 s. The wave power in the three components were then combined by summation in quadrature. Using the same method, Smith, Rae, Forsyth, Watt, and Murphy (2020) found 175 examples of exponential magnetic wave power increases in the magnetotail that were mirrored by similar observations at their conjugate location on the ground. These magnetic ULF wave activations are henceforth assumed to be the in-situ magnetic signature of a near-Earth plasma sheet process (cf., Smith, Rae, Forsyth, Watt, Murphy, & Mann, 2020), active at substorm onset (Forsyth et al., 2015), that is occurring close to the THEMIS spacecraft. These magnetic ULF wave power increases therefore provide a suitable timing benchmark from which to evaluate the evolution of plasma sheet conditions in the near-Earth magnetotail at substorm onset. For our analysis we further require:

- The exponential increase in magnetic wave power to be greater than one order of magnitude.
- The average ion plasma β to be greater than 1.
- A 30 min of quiet (e.g., by eye consistently low wave power representing an approximate noise floor) prior to the exponential increase in wave power.
- Combined plasma moments to be available from 30 min prior to the wave power increase until 15 min afterward.

These requirements ensure: that significant magnetic ULF wave power has been observed and the spacecraft is close to the "onset location" (cf., Smith, Rae, Forsyth, Watt, Murphy, & Mann, 2020); the spacecraft are consistently located within the magnetotail plasma sheet; that pre-onset changes are not related to changes in the spacecraft's magnetospheric location (e.g., through the plasma sheet boundary layer) or previous magnetospheric activity; that sufficient data are available for the analysis to proceed. These criteria were fulfilled by a total 68 intervals of data, which form the basis of our statistical study. Though this is a substantial reduction from the original 175 intervals, these represent a pristine data set with which we can examine the conditions surrounding wave power excitation at substorm onset.

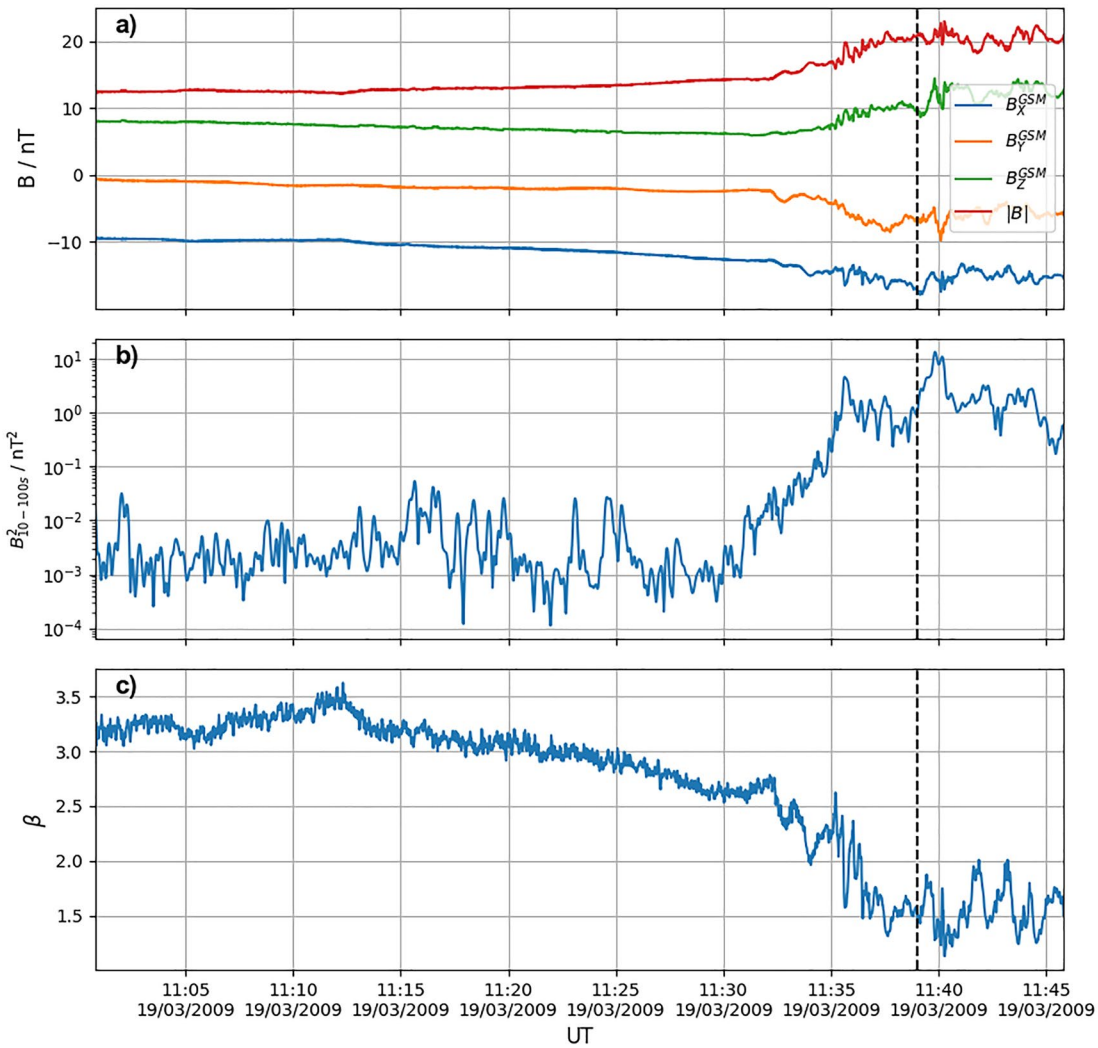

Figure 1. An example interval observed by Time History of Events and Macroscale Interactions during Substorms-D on the 19 March 2009 showing: the magnetic field in the Geocentric-Solar-Magnetospheric (GSM) system (a), the wave power (b), and the plasma β (c). The vertical dashed black line indicates substorm onset as determined from ground based magnetometers (Forsyth et al., 2015).

Figure 1 shows an example of one interval that fulfilled the criteria above. Notably, we see magnetic wave power increase by approximately three orders of magnitude in the minutes prior to substorm onset as determined from ground based magnetometers, that is, using the SOPHIE technique (Forsyth et al., 2015).

3. Results

In this work, we use Superposed Epoch Analyses (SEAs) to evaluate the evolution of the near-Earth plasma sheet around substorm onset. To align these intervals to a consistent epoch, we manually identify the start and the end of the exponential growth of magnetic ULF wave power (in the 10 − 100 s period band). This provides a timing of substorm onset that is local to the spacecraft. This is in contrast to the use of an auroral index to determine substorm onset, which provides a global onset time that is generally within ±15–20 min of onset determined through auroral images (Forsyth et al., 2015). As we will show, the local timing allows us to clearly distinguish pre- and post-onset conditions at the spacecraft location.

We will examine the observations before, during and after the intervals of exponential magnetic wave growth. To enable comparison between events and reduce aliasing effects, we modify the time series such that all events have the same wave growth interval. We stretch or shrink the observed wave power growth interval and resample

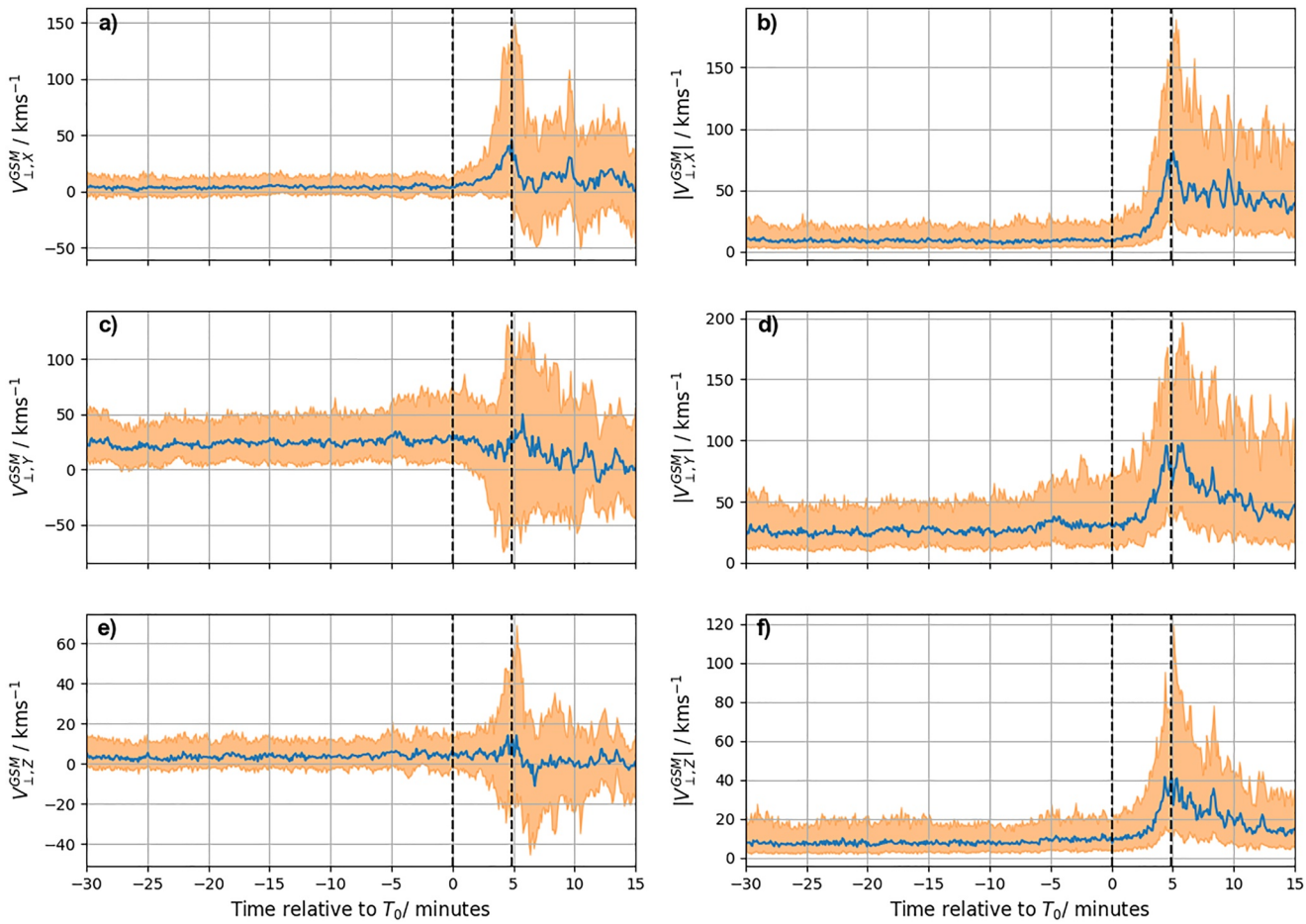

Figure 2. Superposed Epoch Analyses of the plasma velocity perpendicular to the magnetic field that was observed by the Time History of Events and Macroscale Interactions during Substorms spacecraft during 68 intervals around substorm onset, from 30 min prior to the start of the wave growth, until 15 min afterward. The left panels (a, c, e) show the perpendicular plasma velocities in the Geocentric-Solar-Magnetospheric (GSM) system, while the right panels (b, d, f) show the absolute velocities in the same coordinate system. The blue line shows the median of the intervals, while the orange shading represents the 25th and 75th percentiles (i.e., the lower and upper quartiles). T_0 here is defined as the start of the Ultra-Low Frequency (ULF) wave power growth, while the black dashed lines indicate the start and peak of the ULF wave growth; the epochs to which the intervals are aligned.

as required (e.g., Murphy et al., 2018; Walach & Grocott, 2019). The start of the exponential wave growth is then assigned as $T = 0$, while the peak of the wave growth is fixed to the mean of the growth time, in this case 4 min and 50 s. Before and after this interval the time series is unaltered. The distribution of exponential ULF wave growth intervals is shown in Figure A1.

3.1. Flows

We first examine the plasma flows in the magnetotail in the period around the magnetic ULF wave growth. Figure 2 shows SEAs of the plasma velocity perpendicular to the magnetic field, with the time defined: $T = 0$ at the start of the exponential ULF wave power growth, $T = 4.84$ min at the peak wave power. The perpendicular plasma flow is utilized in order to remove any impact from field aligned plasma flows that may be present during this time. Figures 2a, 2c and 2e show SEAs of the perpendicular plasma velocity, while Figures 2b, 2d and 2f show the absolute perpendicular plasma velocity.

Prior to the ULF wave growth we see small flows, predominantly in the positive Y_{GSM} direction, with a magnitude approximately 20 kms^{-1}. Then, at start of the ULF wave growth, we see evidence for increasing flows in all three directions. In the X_{GSM} direction we see planetward flows that rise over the few minutes of wave power growth, peaking at the same time as the ULF wave power (i.e., at ~4 min and 50 s). This flow then drops off quickly

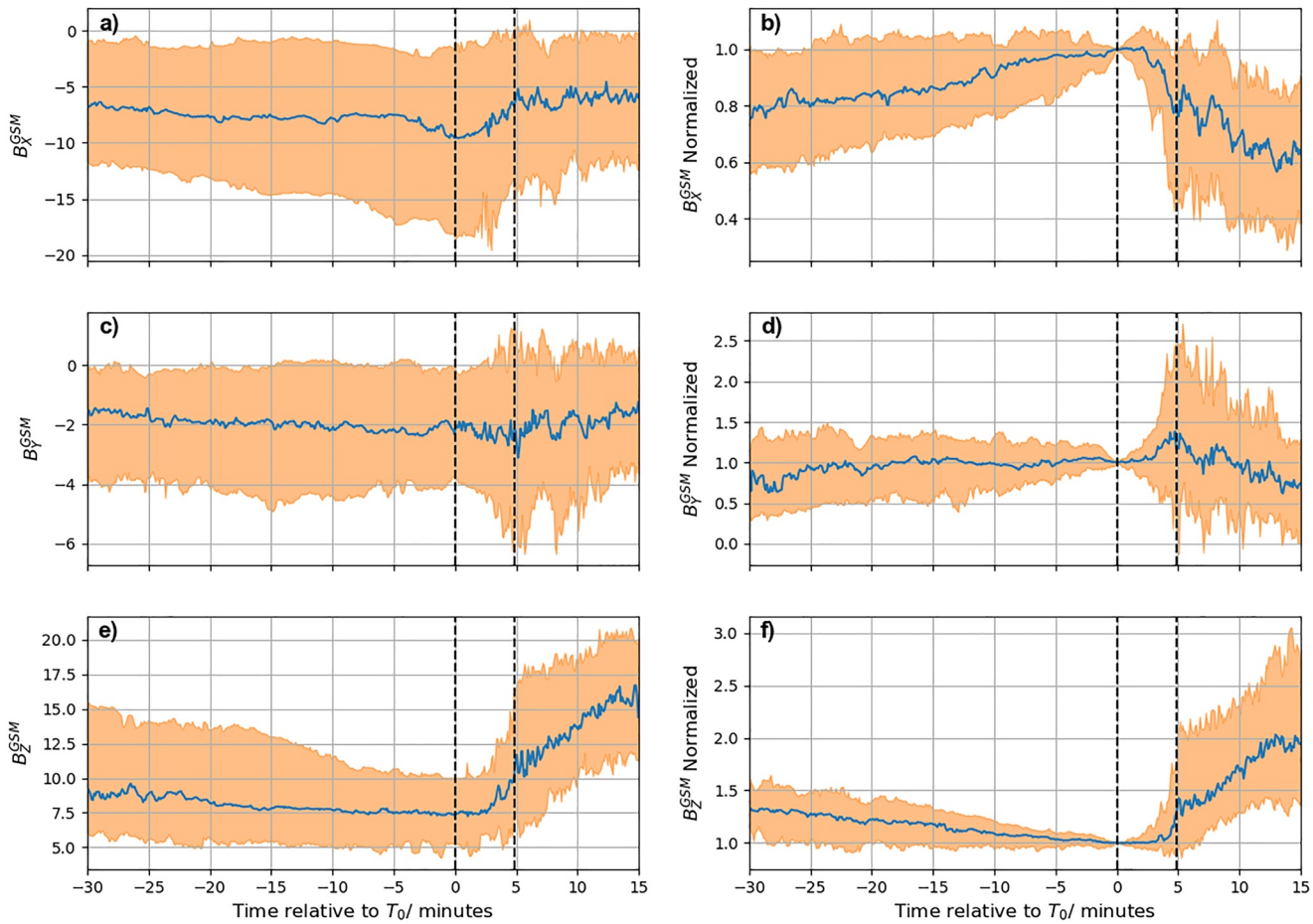

Figure 3. Superposed Epoch Analyses of the magnetic field observed by the Time History of Events and Macroscale Interactions during Substorms spacecraft, in a similar format to Figure 2. The left panels (a, c, e) show the three Geocentric-Solar-Magnetospheric (GSM) components of the magnetic field, while the right panels (b, d, f) show these same intervals normalized to the value of the magnetic field at $T = 0$.

after the peak, potentially exhibiting some oscillatory behavior. In Figure 2b, in the Y_{GSM} direction we see that the quartiles increase during the wave growth interval, though the median remains constant. On the right, in the absolute velocity, we see strong growth in $|V_{\perp,Y}^{\mathrm{GSM}}|$ during the wave growth. This combination of observations suggests that there are approximately equal examples of increasing positive and negative $V_{\perp,Y}^{\mathrm{GSM}}$ during the wave growth. Meanwhile, in $V_{\perp,Z}^{\mathrm{GSM}}$ we see a similar pattern to that in $V_{\perp,Y}^{\mathrm{GSM}}$, though the magnitudes are smaller by a factor of approximately three. This suggests growing velocities in $V_{\perp,Z}^{\mathrm{GSM}}$, again with roughly the same number of positive and negative examples.

3.2. Field Geometry

Next, we examine the changing magnetic field geometry in the interval around substorm onset. Figure 3 shows SEAs of the magnetic field in a similar format to Figure 2. Figures 3a, 3c and 3e show the observed magnetic field. There is a fairly large spread of magnetic field values in each panel, indicated by the breadth of the orange quartiles. This spread could be due to the relative locations of the spacecraft and the current sheet, and also due to the location of the spacecraft within the magnetotail during each event. Therefore, Figures 3b, 3d and 3f show the same intervals but normalized to the value of the magnetic field observed at $T = 0$. This permits a better comparison between the 68 intervals, and allows examination of the changes around the time in which the wave power begins to increase.

Figures 3b and 3f show that in the 30 min prior to the wave power growth we see an increase in B_X^{GSM} and a reduction in B_Z^{GSM}. These changes are gradual, but amount to a change of approximately 20% in both magnitudes.

In contrast, the changes in B_Y^{GSM} are relatively small prior to the wave power growth. During the period in which the wave power is growing, that is, $T = 0$–4.8 min, we see a marked decrease in B_X^{GSM} and increases in B_Y^{GSM} and B_Z^{GSM}. The median field in this time period shows changes of between 20% and 50%. Following the peak of the wave power, that is, after $T = 4.8$ min, B_X^{GSM} continues to decrease while B_Z^{GSM} increases. Meanwhile, B_Y^{GSM} gradually returns toward its original values. All three components of the field appear more variable in this interval, contrasting with the character of the field in the 30 min prior to the increase in wave power.

3.3. Local Energy Density

We now examine the local energy density in the near-Earth magnetotail at substorm onset to further our understanding as to where the energy we ultimately observe as ULF waves may originate. Local energy should be conserved according to:

$$\frac{\partial W_{\mathrm{Total}}}{\partial t} + \nabla \cdot \mathbf{S} = 0 \tag{1}$$

where W_{Total} is the total local energy and S is the flow of energy into the region (a combination of Poynting and advected energy flux). From the data it is not possible to calculate $\nabla \cdot \mathbf{S}$, but nonetheless Equation 1 provides a useful framework with which to understand the observed local energy density. We define the total energy density (U_{Total}) as:

$$U_{\mathrm{Total}} = U_{\mathrm{Field}} + \sum_S U^S_{\mathrm{Kinetic}} + \sum_S U^S_{\mathrm{Thermal}} + U_{\mathrm{Waves}} \tag{2}$$

where the plasma kinetic and thermal terms are summed over the species (S). Specifically, the species considered in this work are protons and electrons. Due to measurement limitations we do not consider the contribution of heavier ions. The energy density of the field is defined as:

$$U_{\mathrm{Field}} = \frac{|\mathbf{B}|^2}{2\mu_0} \tag{3}$$

where μ_0 is the permeability of free space. The separate components of the field are combined by summation in quadrature. To ensure that we do not double count the contribution of any ULF waves present in the magnetic field measurements we low pass filter the magnetic field (for periods greater than 100 s). We then define the plasma kinetic energy density as:

$$U^S_{\mathrm{Kinetic}} = \frac{1}{2} n_S m_S u_S^2 \tag{4}$$

where n_S, m_S, and u_S are the number density, mass and flow speed of the species S, when calculating the total energy density the velocity is low pass filtered (again to prevent double counting of the wave perturbations). Meanwhile, the thermal energy is defined as:

$$U^S_{\mathrm{Thermal}} = \frac{1}{2} n_S k_B \left(T^S_{\perp,1} + T^S_{\perp,2} + T^S_{\parallel} \right) \tag{5}$$

where k_B is the Boltzmann constant and $T^S_{\perp,1}$, $T^S_{\perp,2}$, and $T^S_{\parallel}$ are the temperatures of the species S, perpendicular and parallel to the magnetic field. Then, from Stix (1992) the energy density of the waves can be defined as:

$$U_{\mathrm{Waves}} = \frac{1}{4} \left(\frac{|\mathbf{B}|^2_{\mathrm{Waves}}}{\mu_0} + \epsilon_0 \mathbf{E} \frac{\delta}{\delta \omega} (\omega \epsilon_{ij}) \mathbf{E}^* + nm \mathbf{u}^2_{\mathrm{Waves}} \right) \tag{6}$$

where $|\mathbf{B}|_{\mathrm{Waves}}$ is the field associated with the wave perturbation, $\mathbf{E}$ is the wave electric field, ϵ_0 and μ_0 are the permittivity and permeability of free space, ϵ_{ij} is the Hermitian part of the permittivity tensor, and $\mathbf{u}_{\mathrm{Waves}}$ is the velocity associated with the waves. Due to measurement limitations (and the relative mass difference) we only consider the velocity perturbation associated with ions, neglecting the electron contribution. For low frequency waves ($\omega \ll \Omega_i$, where Ω_i is the ion gyrofrequency) we can write Equation 6 as:

$$U_{\mathrm{Waves}} \approx \frac{|\mathbf{B}|^2_{\mathrm{Waves}}}{2\mu_0} + nm \mathbf{u}^2_{\mathrm{Waves}} \tag{7}$$

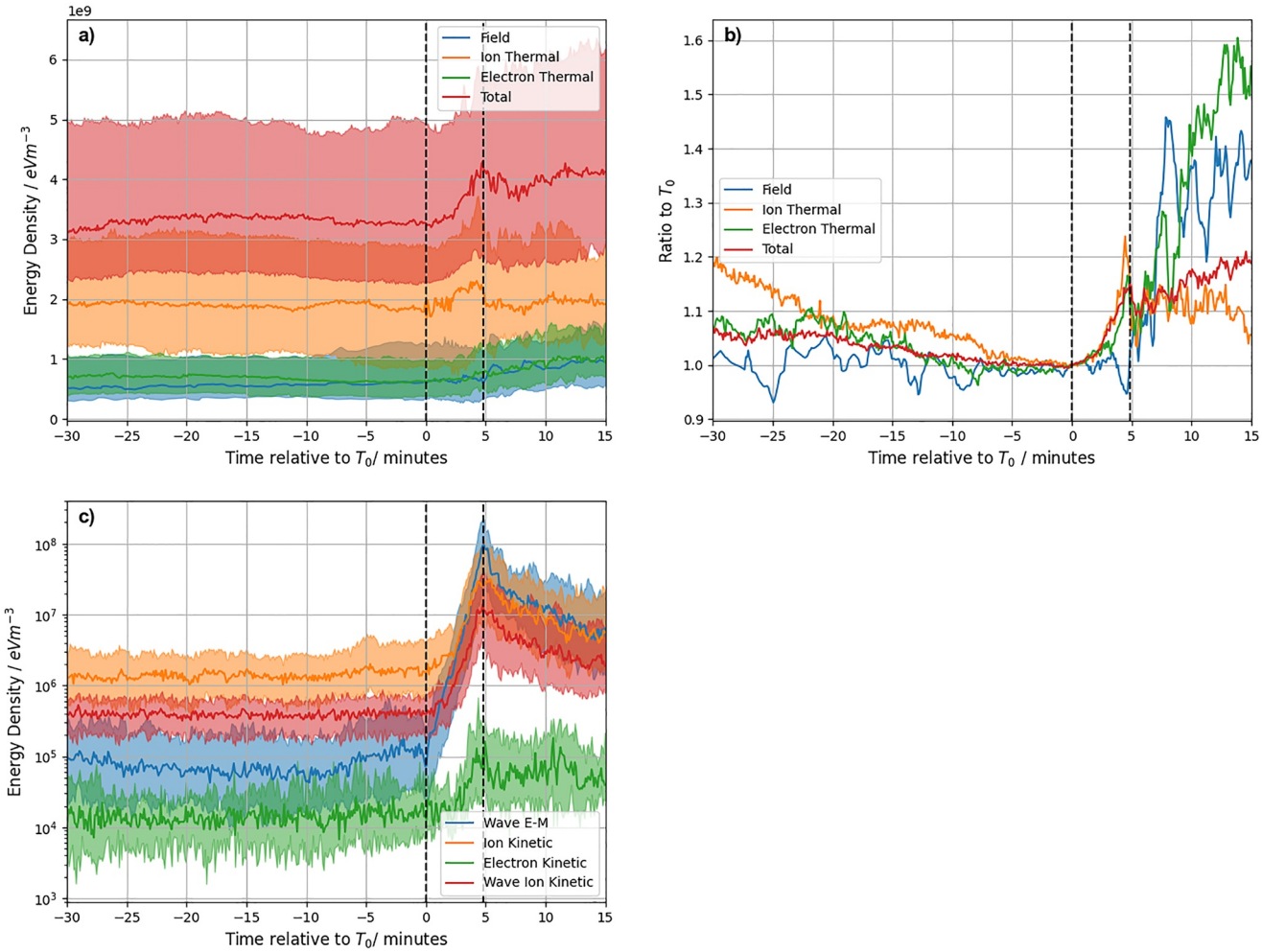

Figure 4. Superposed Epoch Analyses of the local energy density in a similar format to Figures 2 and 3. The top panel (a) shows the total energy density as well as that recorded for the field and thermal plasma. The right panel (b) shows the median change relative to T_0 of the parameters in panel (a). No quartiles are shown to improve the clarity of the panel. The lower panel (c) shows the energy densities of the electromagnetic and ion kinetic wave and bulk ion kinetic, now on a logarithmic scale.

where the two terms on the right now represent the electromagnetic and kinetic components of the wave energy density. We calculate $|\mathbf{B}|_{\text{Waves}}$ and $\mathbf{u}_{\text{Waves}}$ using a bandpass filter between 10 and 100 s for each component, before combining them by summation in quadrature. Figure 4 then shows SEAs of the local energy density and its components in the time around the exponential growth in wave power. Figure 4a shows SEAs of the bulk parameters, while Figure 4b shows the median changes in the bulk parameters relative to $T = 0$ to provide a more direct comparison. Figure 4c then displays SEAs of the flow and wave related parameters (in which the electromagnetic and kinetic terms have been shown separately), which vary over several orders of magnitude. We note that the bandpass filtering was performed prior to the time warping of the interval of wave growth and that the plotted ion kinetic energy is the total ion kinetic energy and therefore includes the contribution of the waves for comparative purposes (though the total energy does not double count the wave ion kinetic energy).

The energy densities are relatively steady leading up to the interval in which the electromagnetic and kinetic wave power grows. This is likely a result of the selection criteria in Section 2: we are only considering those substorms that are preceded by quiet conditions in the magnetotail. From Figure 4b, the total, ion thermal and electron thermal energies show small (~5%–20%) decreases during this time. Meanwhile, the consistent levels of the wave electromagnetic and kinetic energy densities in Figure 4c likely represent the noise floor of these measurements, and suggest that this is lower for the magnetic field measurements.

During the clear electromagnetic wave power growth interval (T = 0–4.8 min), we see a strong increase in the electromagnetic energy density of around three orders of magnitude. The wave kinetic ion energy density (in red)

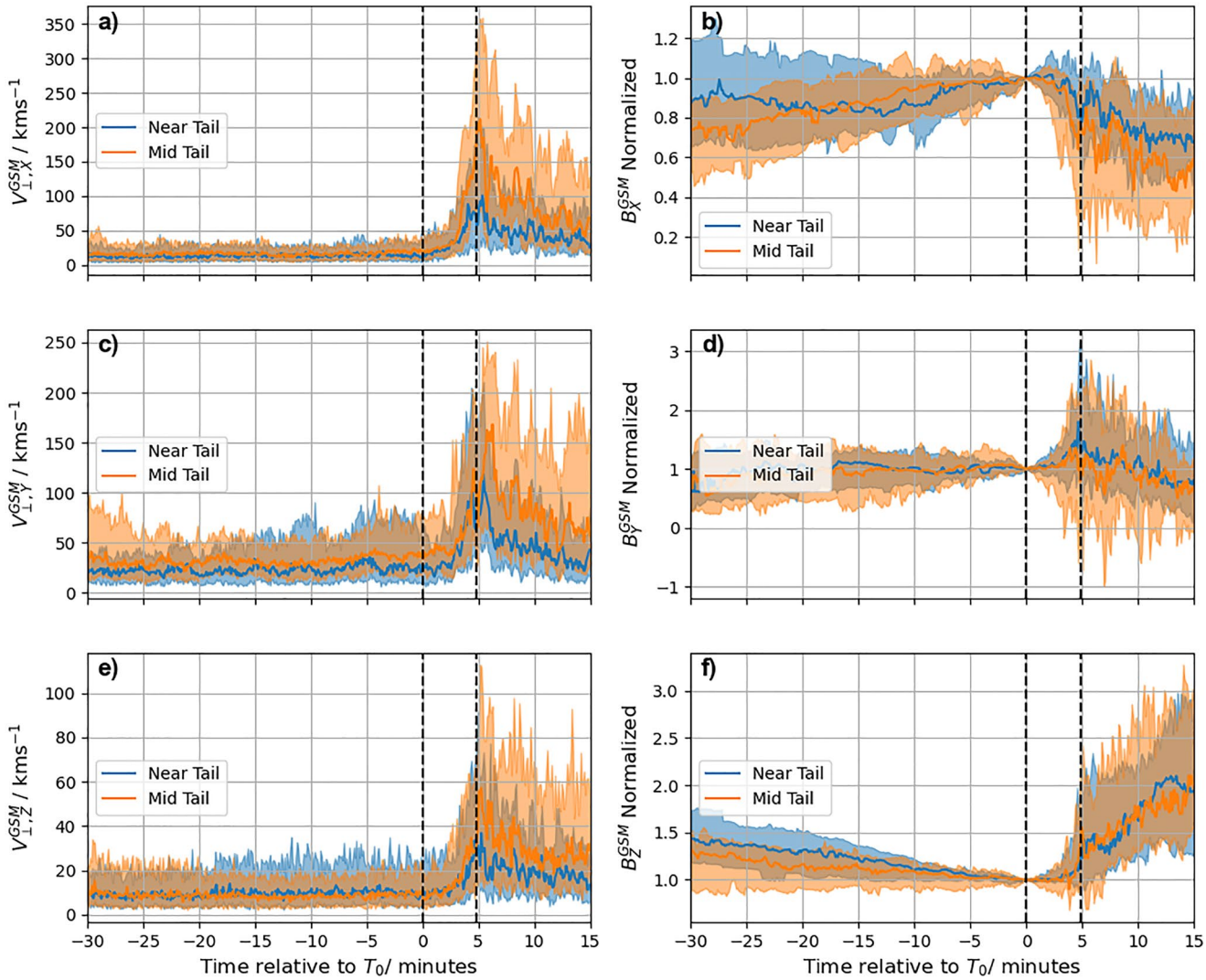

Figure 5. Superposed Epoch Analyses split by downtail distance in a similar format to Figures 2 and 3. The left panels (a, c, e) show the absolute perpendicular plasma flow velocities in the Geocentric-Solar-Magnetospheric (GSM) system, while the right panels (b, d, f) show the three GSM components of the magnetic field, normalized to the value at $T = 0$. The "Near Tail" (blue) here is defined as between $-7.5 \leq X_{\mathrm{GSM}} \leq -10\ R_E$, while the "Mid Tail" (orange) is between $-10 \leq X_{\mathrm{GSM}} \leq -12.5\ R_E$.

also increases in this interval, from its slightly higher noise floor. This indicates that we resolve the MHD waves in both the magnetic field and in the plasma flows. Also during this time interval we see an increase in the bulk ion kinetic energy density, that is around a factor of 2–3 greater than that in the wave ion kinetic energy density. This suggests that while some of the observed flows are related to the growing waves, there are also significant bulk motions of the plasma that increase during this time. Significantly, we also see that the total energy density increases during this period of wave growth, but that it cannot be explained purely by the growing wave or flow energies.

3.4. Spatial Differences

The intervals studied so far have been observed between $-7.5\ R_E$ and $-12.5\ R_E$ from the Earth, a fairly large spread in a region of the tail that shows large spatial variations and gradients. We now break down the observations into two main categories, those observed either side of $-10\ R_E$; terming those closer to the planet as occurring in the "Near Tail," and those beyond as being observed in the "Mid Tail." Figure 5 shows SEAs for the two categories of events in blue and orange respectively. The left of Figure 5 shows SEAs for the absolute

perpendicular plasma velocity observed in the GSM coordinate system. In these panels, we can see that the shapes of the velocity profiles are similar in both the near and far-tail. However, the magnitude of the peak velocities are about twice as large in the mid-tail.

Regarding the field geometry, the right of Figure 5 shows the magnetic field normalized to the field observed at $T = 0$, once more split by the distance downtail. While the trends in $V_{\perp,Y}^{\mathrm{GSM}}$ and $V_{\perp,Z}^{\mathrm{GSM}}$ are similar in both regions of the tail, the timing of the increase in B_X^{GSM} appears to depend on where in the tail it is observed. In the mid-tail we see the increase in B_X^{GSM} roughly 10–20 min before the wave power begins to increase. In contrast, in the near-tail we only see the increase in B_X^{GSM} about 10 min prior to the wave power increase.

4. Discussion

In this study, we have used SEAs to examine the changes in the near-Earth magnetotail around intervals of exponential ULF wave growth at substorm onset. We identified the start and end of the observed ULF wave growth, and used these as fixed epochs to normalize the time series. While this is excellent at resolving changes around the identified times, this processing will result in some aliasing effects. Within the wave growth interval it means we are unlikely to resolve wave-like fluctuations, both due to the lack of a consistent dominant period (e.g., Murphy et al., 2011), and the dynamic time normalization employed. Moreover, if changes occur significantly before or after the identified epochs then they will not be resolved. Below, we discuss the dynamics of the magnetotail prior to, during and after the increase in ULF wave power, as well as the implications of these dynamics in the evolution of the magnetotail during the substorm cycle.

4.1. Observations Prior to the Wave Power Increase

First, we will discuss the conditions in the 30 min before the exponential 10–100 s wave power increase. The plasma flows observed in this time are relatively small, predominantly in $V_{\perp,Y}^{\mathrm{GSM}}$. Given the pre-midnight preference for these events (Smith, Rae, Forsyth, Watt, & Murphy, 2020), the observation of small, positive $V_{\perp,Y}^{\mathrm{GSM}}$ flows likely represents enhanced convectional flows during the substorm growth phase, directed azimuthally, and ultimately toward the dayside (e.g., Sun et al., 2017).

Interestingly, we do not see evidence in this time before the wave growth of an increase in plasma sheet pressure. Canonically, it is expected that during the substorm growth phase open magnetic flux is stored within the magnetotail lobes (Baker et al., 1985; Caan et al., 1978). This causes the tail to flare, increasing the solar wind ram pressure on the tail, and thereby increasing the lobe energy density (Baker et al., 1997; Caan et al., 1975; Coxon et al., 2018), and equivalently pressure. This increased lobe pressure must be balanced by larger pressure within the magnetotail plasma sheet (Forsyth et al., 2014; Wang et al., 2004; Yue et al., 2015). On the other hand, some studies have noted little or no increase in plasma sheet pressure during the growth phase (Kistler et al., 1993; Snekvik et al., 2012). A recent study using THEMIS data found that plasma pressure decreased in the plasma sheet before 40% of the substorms studied (Sun et al., 2017). This was inferred to be a result of the enhanced transport of magnetic flux from the near-tail region to the dayside magnetosphere, termed Magnetic Flux Depletion (M. Hsieh & Otto, 2015; M.-S. Hsieh & Otto, 2014).

In the magnetic field, we see consistent evidence of the stretching of the magnetic field, with reduction in the B_Z^{GSM} and increase in the B_X^{GSM} components of the magnetic field. However, we do not see statistical evidence of consistent tail flaring (i.e., increasing B_Y^{GSM}) during these intervals, perhaps as we are sampling regions relatively close to the center of the magnetotail. We find that the timing of the tail stretching, inferred primarily through the increase in B_X^{GSM}, appears to occur about 10 min earlier in the mid-tail ($-10 \leq X_{\mathrm{GSM}} \leq -12.5\ R_E$), than in the near-tail ($-7.5 \leq X_{\mathrm{GSM}} \leq -10\ R_E$). This difference in timing could suggest that regions of the plasma sheet more distant from the Earth stretch more easily, and that this process takes time to penetrate closer toward the Earth. However, once the inner plasma sheet has stretched then the inner region rapidly destabilizes.

4.2. Observations During the Wave Power Increase

We see evidence of strong peaks in the observed perpendicular plasma velocity at the time of peak wave power. This is true for all three components of the velocity, though notably we see a peak in $V_{\perp,X}^{\mathrm{GSM}}$ with a median of around 80 kms^{-1}, indicating strong Earthward flows at this time. The median peak flow in $|V_{\perp,Y}^{\mathrm{GSM}}|$ is comparable

at approximately 80–90 kms^{-1}, while the median peak flow in Z_{GSM} is much smaller at ∼40 kms^{-1}. We find that the magnitude of the flow is dependent upon location within the magnetotail, with the peak flows being up to 100% faster in the mid-tail ($-10 \leq X_{GSM} \leq -12.5\ R_E$) than in the near-tail ($-7.5 \leq X_{GSM} \leq -10\ R_E$). A similar result was reported by Fukui et al. (2019) in their survey of the near-Earth magnetotail during the growth phase of substorms. Fukui et al. (2019) attributed these flows and observations to either near-Earth magnetic reconnection (e.g., Angelopoulos et al., 2008), or the relaxation of the current sheet toward the Earth around substorm onset (e.g., Machida et al., 2009, 2014). Assuming an Earthward velocity of 80 kms^{-1}, any flow resulting from reconnection at ∼20 R_E would require 13–14 min to travel 10 R_E to the location of the spacecraft. This, combined with the relatively slow increase in velocity during the growth of ULF wave power (cf., dipolarization fronts, Runov et al., 2009; Schmid et al., 2016) make this unlikely to be the direct result of reconnection from $X_{GSM} \sim 20\ R_E$. Nonetheless, previous works have strongly associated "flow bursts" and ULF waves (e.g., Keiling & Takahashi, 2011; Kim et al., 2007). Interestingly, when we compared the energy density related to the bulk motions of the plasma with that associated with growing 10–100 s MHD waves (Figure 4b), we can see that a sizable portion of the kinetic energy of the flows is associated with the waves, and not just bulk motions of the plasma.

The flows in $V_{\perp,Y}^{GSM}$ were noticeably symmetric, with an approximately even split between positive and negative flow observations. This caused the initial SEA analysis to return no median flow (e.g., Figure 2c), though when the absolute value of the velocity was taken the significant median flow of ∼100 kms^{-1} was revealed. This could be due to the location of the spacecraft relative to substorm onset, for example, displaced east or west. We can examine the scale size of the flows in $V_{\perp,Y}^{GSM}$ using examples when two of the THEMIS spacecraft both observed the ULF wave growth during the same substorm onset. We find a total of 12 substorms for which these multi-point observations were possible. During these intervals the THEMIS D and E spacecraft were typically separated (primarily in azimuth) by approximately 1 R_E. In 5 out of 12 (∼40%) of these substorms the flows in Y_{GSM} were in different directions, and divergent. These observations indicate that the significant $V_{\perp,Y}^{GSM}$ flows are not in a single global direction, and provides length scales that may be compared with predictions of instabilities in the magnetotail (cf., Oberhagemann & Mann, 2020; Panov et al., 2020, 2022; Viñas & Madden, 1986; Voronkov et al., 1997).

When considering the local energy density in the interval it is striking that the median total energy density increases by ∼15% during the period of wave power growth. If the waves had a local source, for example, from an electron temperature anisotropy (Walsh et al., 2011), then we might expect to see this reflected in the data, with a decrease in one of the other measures of energy density (e.g., the electron thermal energy density), in order to balance the increase in wave energy density. As we do not see a clear decrease in any of the bulk energy densities, we do not see clear evidence for a local energy source. Further, from the standpoint of the conservation of energy (cf., Equation 1) this local increase in energy density leaves two possibilities. The first is that the volume of the region has reduced in space—that is, while U_{Total} has increased the plasma sheet is thinner such that the total energy (W_{Total}) of the region is constant. The second possibility is that energy has been added to the region from an external source (i.e., $\nabla \cdot \mathbf{S}$ is negative in Equation 1). We note that neither of these possibilities necessarily excludes the other.

Figure 4b shows that the total energy density increase cannot be attributed to increases in wave (electromagnetic or kinetic) or bulk ion kinetic energy density, which are approximately an order of magnitude too small to account for the change in the total energy density. However, we see ∼10%–20% increases in the local ion and electron thermal energy density. Closer inspection (not shown) reveals this to be due to increasing plasma temperature, and not plasma density. As the density has not appreciably increased then the first suggestion above—that the local "region" has reduced in size (conserving energy given a larger local energy density)—would not be favored. Therefore, we suggest that it is likely that the energy has come from elsewhere in the magnetotail, for example, through advection (i.e., $\nabla \cdot \mathbf{S}$ is negative in Equation 1). The temperature increases appear isotopic, with no clear pitch angle dependence.

We might assume that the exponentially growing MHD waves are driven by an instability in the near-Earth magnetotail, consistent with previous works that have provided strong observational evidence (e.g., Kalmoni et al., 2018; Rae et al., 2010, 2012). As these waves grow, we find evidence for an increase in total energy density at the spacecraft. Though we lack the spacecraft coverage to probe the detailed nature of gradients in the near-Earth magnetotail, a gradient driven instability would manifest to reduce the gradient that created it, either

through plasma mixing or heating. Thus these observations may broadly support the notion of a temperature or pressure gradient driven instability (e.g., Cheng, 2004; Lee et al., 1998; Oberhagemann & Mann, 2020; Viñas & Madden, 1986; Voronkov et al., 1997; Zhu et al., 2004).

4.3. Observations After the Wave Power Increase

After the peak wave power (i.e., after $T = 4.8$ min), we see further changes in the near-Earth magnetotail. Significantly, the tail becomes more dipolar, as evidenced by the reducing values of B_X^{GSM} and increasing B_Z^{GSM}. This likely corresponds to the dipolarization of the magnetotail at onset, however the broad spread (represented by the quartile ranges in Figures 3b and 3f) suggests there may be significant time aliasing in the dipolarization. If true, this would suggest that the dipolarization of the near-Earth tail occurs independently (in time) of the ULF wave process, and not at a fixed interval following the peak ULF wave power. Future work should investigate the absolute timing offset between near-Earth ULF wave processes and the dipolarization of the magnetotail. We note that there does not appear to be a time offset between the near-tail and mid-tail when considering B_Z^{GSM}, while there may be a faster change in the mid-tail when considering B_X^{GSM}.

The strong earthward flows (in $V_{\perp,X}^{\mathrm{GSM}}$) observed appear to subside in an oscillatory manner, with periods of the order of ∼5 min. Similar observations were also made by Fukui et al. (2019), and could represent the bouncing of the earthward flows (e.g., Ohtani et al., 2009; Panov et al., 2010). While the mid-tail observations ($-10 \leq X_{\mathrm{GSM}} \leq -12.5\ R_E$) showed stronger flows, we also see that these subside more slowly and show greater variability. If the spacecraft were to observe incoming BBFs from the mid-tail (Angelopoulos et al., 1992), then they would likely be aliased in this interval, and present the observed broadly increased $V_{\perp,X}^{\mathrm{GSM}}$. The larger velocity in the mid-tail ($-10 \leq X_{\mathrm{GSM}} \leq -12.5\ R_E$), might also be explained by BBFs, fewer of which may be expected to penetrate as close to the Earth, or that they would slow as the gradients in the magnetotail increase closer to the planet.

The local energy density is enhanced by approximately 20% in the time period following the ULF wave peak, and we find that this is mostly attributable to increases in magnetic field and ion and electron thermal energy densities. This likely represents the more dipolar and hotter magnetospheric configuration following the substorm onset.

5. Summary

In this work, we have analyzed THEMIS observations of the near-Earth magnetotail at substorm onset. We have aligned the intervals using local observations of exponential magnetic ULF wave power increase (with periods between 10–100 s), which have been found to be one of the first phenomena observed at substorm onset. Ordering the intervals by the start and peak of the wave power increase has shown that these times denote points of inflection in a number of the parameters of the near-Earth magnetotail.

In the 30 min prior to the exponential growth of ULF waves, the magnetic field in the near-Earth magnetotail is found to stretch, with increases in B_X^{GSM} and reductions in B_Z^{GSM}. In this time convectional and predominately azimuthal plasma flows dominate. No statistical increase in plasma sheet energy density or magnetotail flaring is observed.

We then observe exponential increases in electromagnetic ULF wave power, with a mean duration of 4.84 min. During this time, the median electromagnetic wave energy density increases by approximately three orders of magnitude. We see strong increases in perpendicular plasma flow velocity (and energy density) during this time, peaking at a similar time to the ULF wave power. Around a third to half of the ion kinetic energy density is found to be attributable to the growing waves, while the remainder is associated with bulk motions of the plasma. The ion flow is predominantly found to be in the earthward and azimuthal directions. The flows are found to be faster in the mid-tail ($-10 \leq X_{\mathrm{GSM}} \leq -12.5\ R_E$) than in the near-tail ($-7.5 \leq X_{\mathrm{GSM}} \leq -10\ R_E$). When multiple spacecraft are compared (spaced by ∼1 R_E) the flows may be in the same direction, or diverge, depending on the event considered—evidencing the relatively small-scale size of these flows. The local energy density is found to increase while the ULF waves are growing, suggesting either external energy source or a reduction in volume of the near-Earth plasma sheet. This increase is primarily attributable to an increase in the plasma temperature, perhaps indicating enhanced plasma heating or mixing. These observations provide empirical constraints that can be compared to theoretical expectations of the processes active in the unstable magnetotail at substorm onset.

Following the increase in wave power we see the dipolarization of the magnetotail, and the subsidence of plasma flow. The local energy density is enhanced by approximately 20% compared to before; primarily due to enhanced magnetic field and plasma thermal energy densities.

Appendix A: Durations of Wave Power Growth

The wavepower growth intervals are normalized such that they have the same duration (discussed in Section 3), chosen to be the mean duration. The original distribution of wave power growth durations is shown in Figure A1, and can be seen to range from one to 14 min, with a mean of 4.84 min.

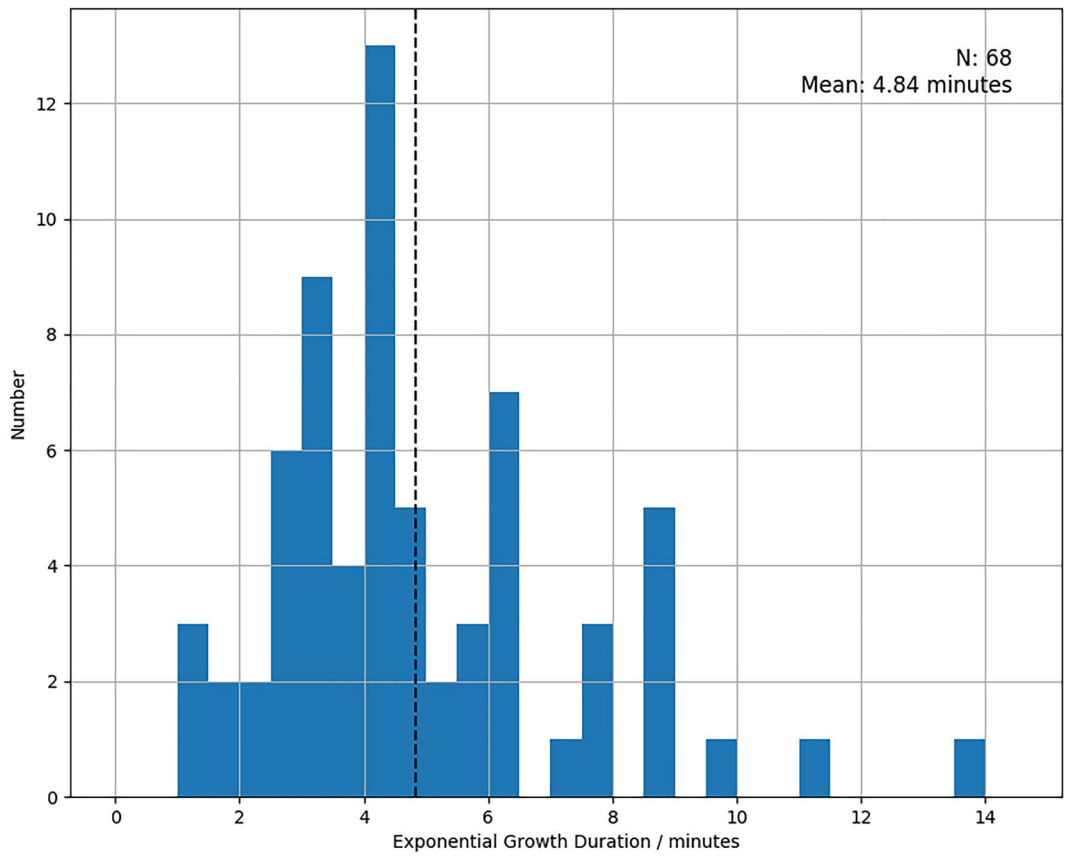

Figure A1. Histogram showing the duration of exponential wave power growth (10–100 s) observed in the 68 intervals of the study.

Data Availability Statement

THEMIS data are available at http://themis.ssl.berkeley.edu/data/themis/. The SuperMAG geomagnetic indices can be found at http://supermag.jhuapl.edu. The analysis in this paper was performed using python, including the pandas (McKinney, 2010), NumPy (Walt et al., 2011), SciPy (Virtanen et al., 2020), and Matplotlib (Hunter, 2007) libraries.

Acknowledgments
The authors acknowledge the NASA contract NAS5-02099 and V. Angelopoulos for use of data from the THEMIS Mission. Specifically, C. W. Carlson and J. P. McFadden for use of Electrostatic Analyzer data; D. Larson and the late R. P. Lin for use of Solid State Telescope data; and K. H. Glassmeier, U. Auster and W. Baumjohann for the use of FGM data provided under the lead of the Technical University of Braunschweig and with financial support through the German Ministry for Economy and Technology and the German Center for Aviation and Space (DLR) under contract 50 OC 0302. AWS and CF were supported by the STFC Consolidated Grant ST/S000240/1, and the NERC Grants NE/P017150/1 and NE/V002724/1. AWS was also supported by NERC Independent Research Fellowship NE/W009129/1, while CF was also supported by the NERC Independent Research Fellowship NE/N014480/1. IJR was supported by STFC Consolidated Grant ST/V006320/1. KRM is partially supported by NERC Grant NE/V002554/2.

References

Akasofu, S.-I. (1964). The development of the auroral substorm. *Planetary and Space Science*, *12*(4), 273–282. https://doi.org/10.1016/0032-0633(64)90151-5

Akasofu, S.-I. (1977). Physics of magnetospheric substorms. Research supported by NSF, NASA, ERDA, and U.S. Air Force (Astrophysics and Space Science Library. Vol. *47*, pp. 619). D. Reidel Publishing Co. Retrieved from http://adsabs.harvard.edu/abs/1977nsf….47….A

Angelopoulos, V. (2008). The THEMIS mission. *Space Science Reviews*, *141*(1–4), 5–34. https://doi.org/10.1007/s11214-008-9336-1

Angelopoulos, V., Baumjohann, W., Kennel, C. F., Coroniti, F. V., Kivelson, M. G., Pellat, R., et al. (1992). Bursty bulk flows in the inner central plasma sheet. *Journal of Geophysical Research*, *97*(A4), 4027. https://doi.org/10.1029/91JA02701

Angelopoulos, V., McFadden, J. P., Larson, D., Carlson, C. W., Mende, S. B., Frey, H., et al. (2008). Tail reconnection triggering substorm onset. *Science (New York, N.Y.)*, *321*(5891), 931–935. https://doi.org/10.1126/science.1160495

Auster, H. U., Glassmeier, K. H., Magnes, W., Aydogar, O., Baumjohann, W., Constantinescu, D., et al. (2009). *The THEMIS fluxgate magnetometer*. Springer. https://doi.org/10.1007/978-0-387-89820-9_11

Baker, D. N., Fritz, T. A., McPherron, R. L., Fairfield, D. H., Kamide, Y., & Baumjohann, W. (1985). Magnetotail energy storage and release during the CDAW 6 substorm analysis intervals. *Journal of Geophysical Research*, *90*(A2), 1205. https://doi.org/10.1029/JA090iA02p01205

Baker, D. N., Pulkkinen, T. I., Hesse, M., & McPherron, R. L. (1997). A quantitative assessment of energy storage and release in the Earth's magnetotail. *Journal of Geophysical Research*, *102*(A4), 7159–7168. https://doi.org/10.1029/96JA03961

Baumjohann, W., Paschmann, G., & Lühr, H. (1990). Characteristics of high-speed ion flows in the plasma sheet. *Journal of Geophysical Research*, *95*(A4), 3801. https://doi.org/10.1029/JA095iA04p03801

Caan, M. N., McPherron, R. L., & Russell, C. T. (1975). Substorm and interplanetary magnetic field effects on the geomagnetic tail lobes. *Journal of Geophysical Research*, *80*(1), 191–194. https://doi.org/10.1029/JA080i001p00191

Caan, M. N., McPherron, R. L., & Russell, C. T. (1978). The statistical magnetic signature of magnetospheric substorms. *Planetary and Space Science*, *26*(3), 269–279. https://doi.org/10.1016/0032-0633(78)90092-2

Chang, T.-F., & Cheng, C.-Z. (2015). Relationship between wave-like auroral arcs and Pi2 disturbances in plasma sheet prior to substorm onset. *Earth Planets and Space*, *67*(1), 168. https://doi.org/10.1186/s40623-015-0334-8

Cheng, C. (2004). Physics of substorm growth phase, onset, and dipolarization. *Space Science Reviews*, *113*(1/2), 207–270. https://doi.org/10.1023/B:SPAC.0000042943.59976.0e

Coxon, J. C., Freeman, M. P., Jackman, C. M., Forsyth, C., Rae, I. J., & Fear, R. C. (2018). Tailward propagation of magnetic energy density variations with respect to substorm onset times. *Journal of Geophysical Research: Space Physics*, *123*(6), 4741–4754. https://doi.org/10.1029/2017JA025147

Donovan, E., Liu, W., Liang, J., Spanswick, E., Voronkov, I., Connors, M., et al. (2008). Simultaneous THEMIS in situ and auroral observations of a small substorm. *Geophysical Research Letters*, *35*(17), L17S18. https://doi.org/10.1029/2008GL033794

Eastwood, J. P., & Kiehas, S. A. (2015). *Origin and evolution of plasmoids and flux ropes in the magnetotails of Earth and Mars*. American Geophysical Union (AGU). https://doi.org/10.1002/9781118842324.ch16

Forsyth, C., Rae, I. J., Coxon, J. C., Freeman, M. P., Jackman, C. M., Gjerloev, J., & Fazakerley, A. N. (2015). A new technique for determining Substorm Onsets and Phases From Indices of the Electrojet (SOPHIE). *Journal of Geophysical Research: Space Physics*, *120*(12), 10592–10606. https://doi.org/10.1002/2015JA021343

Forsyth, C., Watt, C. E. J., Rae, I. J., Fazakerley, A. N., Kalmoni, N. M. E., Freeman, M. P., et al. (2014). Increases in plasma sheet temperature with solar wind driving during substorm growth phases. *Geophysical Research Letters*, *41*(24), 8713–8721. https://doi.org/10.1002/2014GL062400

Friedrich, E., Samson, J. C., & Voronkov, I. (2001). Ground-based observations and plasma instabilities in auroral substorms. *Physics of Plasmas*, *8*(4), 1104. https://doi.org/10.1063/1.1355678

Fukui, K., Miyashita, Y., Machida, S., Miyoshi, Y., Ieda, A., Nishimura, Y., & Angelopoulos, V. (2019). A statistical study of near-Earth magnetotail evolution during pseudosubstorms and substorms with THEMIS data. *Journal of Geophysical Research: Space Physics*, *125*(1), 2019JA026642. https://doi.org/10.1029/2019JA026642

Haerendel, G., & Frey, H. (2021). The onset of a substorm and the mating instability. *Journal of Geophysical Research: Space Physics*, *126*(10), e2021JA029492. https://doi.org/10.1029/2021ja029492

Henderson, M. G. (1994). Implications of Viking imager results for substorm models (PhD Thesis, Dissertation Abstracts International, Volume: 56-01, Section: B, p. 0289). University of Calgary (Canada). Retrieved from http://adsabs.harvard.edu/abs/1994PhDT…….53H

Hones, E. W., Baker, D. N., Bame, S. J., Feldman, W. C., Gosling, J. T., McComas, D. J., et al. (1984). Structure of the magnetotail at 220 R_E and its response to geomagnetic activity. *Geophysical Research Letters*, *11*(1), 5–7. https://doi.org/10.1029/GL011i001p00005

Horvath, I., & Lovell, B. C. (2019). Abnormal subauroral ion drifts (ASAID) and Pi2s during cross-tail current disruptions observed by polar on the magnetically quiet days of October 2003. *Journal of Geophysical Research: Space Physics*, *124*(7), 6097–6116. https://doi.org/10.1029/2019JA026725

Hsieh, M., & Otto, A. (2015). Thin current sheet formation in response to the loading and the depletion of magnetic flux during the substorm growth phase. *Journal of Geophysical Research: Space Physics*, *120*(6), 4264–4278. https://doi.org/10.1002/2014JA020925

Hsieh, M.-S., & Otto, A. (2014). The influence of magnetic flux depletion on the magnetotail and auroral morphology during the substorm growth phase. *Journal of Geophysical Research: Space Physics*, *119*(5), 3430–3443. https://doi.org/10.1002/2013JA019459

Hunter, J. D. (2007). Matplotlib: A 2D graphics environment. *Computing in Science & Engineering*, *9*(3), 90–95. https://doi.org/10.1109/MCSE.2007.55

Kalmoni, N. M. E., Rae, I. J., Murphy, K. R., Forsyth, C., Watt, C. E., & Owen, C. J. (2017). Statistical azimuthal structuring of the substorm onset arc: Implications for the onset mechanism. *Geophysical Research Letters*, *44*(5), 2078–2087. https://doi.org/10.1002/2016GL071826

Kalmoni, N. M. E., Rae, I. J., Watt, C. E. J., Murphy, K. R., Forsyth, C., & Owen, C. J. (2015). Statistical characterization of the growth and spatial scales of the substorm onset arc. *Journal of Geophysical Research: Space Physics*, *120*(10), 8503–8516. https://doi.org/10.1002/2015JA021470

Kalmoni, N. M. E., Rae, I. J., Watt, C. E. J., Murphy, K. R., Samara, M., Michell, R. G., et al. (2018). A diagnosis of the plasma waves responsible for the explosive energy release of substorm onset. *Nature Communications*, *9*(1), 4806. https://doi.org/10.1038/s41467-018-07086-0

Keiling, A., & Takahashi, K. (2011). Review of Pi2 models. *Space Science Reviews*, *161*(1–4), 63–148. https://doi.org/10.1007/s11214-011-9818-4

Kepko, L., McPherron, R. L., Amm, O., Apatenkov, S., Baumjohann, W., Birn, J., et al. (2015). Substorm current wedge revisited. *Space Science Reviews*, *190*(1–4), 1–46. https://doi.org/10.1007/s11214-014-0124-9

Kim, K. H., Takahashi, K., Ohtani, S., & Sung, S. K. (2007). Statistical analysis of the relationship between earthward flow bursts in the magnetotail and low-latitude Pi2 pulsations. *Journal of Geophysical Research*, *112*(A10), A10211. https://doi.org/10.1029/2007JA012521

Kistler, L. M., Baumjohann, W., Nagai, T., & Möbius, E. (1993). Superposed epoch analysis of pressure and magnetic field configuration changes in the plasma sheet. *Journal of Geophysical Research*, *98*(A6), 9249. https://doi.org/10.1029/93JA00630

Lee, L. C., Zhang, L., Otto, A., Choe, G. S., & Cai, H. J. (1998). Entropy antidiffusion instability and formation of a thin current sheet during geomagnetic substorms. *Journal of Geophysical Research*, *103*(A12), 29419–29428. https://doi.org/10.1029/97JA02141

Lui, A. (2004). Potential plasma instabilities for substorm expansion onsets. *Space Science Reviews*, *113*(1/2), 127–206. https://doi.org/10.1023/B:SPAC.0000042942.00362.4e

Lui, A. T. Y., Chang, C.-L., Mankofsky, A., Wong, H.-K., & Winske, D. (1991). A cross-field current instability for substorm expansions. *Journal of Geophysical Research*, *96*(A7), 11389. https://doi.org/10.1029/91JA00892

Machida, S., Miyashita, Y., Ieda, A., Nosé, M., Angelopoulos, V., & McFadden, J. P. (2014). Statistical visualization of the Earth's magnetotail and the implied mechanism of substorm triggering based on superposed-epoch analysis of THEMIS data. *Annales Geophysicae*, *32*(2), 99–111. https://doi.org/10.5194/angeo-32-99-2014

Machida, S., Miyashita, Y., Ieda, A., Nosé, M., Nagata, D., Liou, K., et al. (2009). Statistical visualization of the Earth's magnetotail based on Geotail data and the implied substorm model. *Annales Geophysicae*, *27*(3), 1035–1046. https://doi.org/10.5194/angeo-27-1035-2009

McFadden, J. P., Carlson, C. W., Larson, D., Ludlam, M., Abiad, R., Elliott, B., et al. (2009). *The THEMIS ESA plasma instrument and in-flight calibration*. Springer. https://doi.org/10.1007/978-0-387-89820-9_13

McKinney, W. (2010). Data structures for statistical computing in python. Retrieved from http://conference.scipy.org/proceedings/scipy2010/mckinney.html

McPherron, R. L. (1970). Growth phase of magnetospheric substorms (Vol. *75*). Retrieved from http://citeseerx.ist.psu.edu/viewdoc/download?doi=10.1.1.452.9720%26rep=rep1%26type=pdf

Milling, D. K., Rae, I. J., Mann, I. R., Murphy, K. R., Kale, A., Russell, C. T., et al. (2008). Ionospheric localisation and expansion of long-period Pi1 pulsations at substorm onset. *Geophysical Research Letters*, *35*(17), L17S20. https://doi.org/10.1029/2008GL033672

Motoba, T., Hosokawa, K., Kadokura, A., & Sato, N. (2012). Magnetic conjugacy of northern and southern auroral beads. *Geophysical Research Letters*, *39*(8), L08108. https://doi.org/10.1029/2012GL051599

Murphy, K. R., Bentley, S. N., Miles, D. M., Sandhu, J. K., & Smith, A. W. (2022). Imaging the magnetosphere–ionosphere system with ground-based and in-situ magnetometers. In *Magnetospheric imaging* (pp. 287–340). https://doi.org/10.1016/B978-0-12-820630-0.00002-7

Murphy, K. R., Mann, I. R., Rae, I. J., Walsh, A. P., & Frey, H. U. (2014). Inner magnetospheric onset preceding reconnection and tail dynamics during substorms: Can substorms initiate in two different regions? *Journal of Geophysical Research: Space Physics*, *119*(12), 9684–9701. https://doi.org/10.1002/2014JA019795

Murphy, K. R., Mann, I. R., Rae, I. J., Waters, C. L., Frey, H. U., Kale, A., et al. (2013). The detailed spatial structure of field-aligned currents comprising the substorm current wedge. *Journal of Geophysical Research: Space Physics*, *118*(12), 7714–7727. https://doi.org/10.1002/2013JA018979

Murphy, K. R., Rae, I. J., Mann, I. R., & Milling, D. K. (2011). On the nature of ULF wave power during nightside auroral activations and substorms: 1. Spatial distribution. *Journal of Geophysical Research*, *116*(A5), A00I21. https://doi.org/10.1029/2010JA015757

Murphy, K. R., Rae, I. J., Mann, I. R., Milling, D. K., Watt, C. E., Ozeke, L., et al. (2009). Wavelet-based ULF wave diagnosis of substorm expansion phase onset. *Journal of Geophysical Research*, *114*(A1), A00C16. https://doi.org/10.1029/2008JA013548

Murphy, K. R., Watt, C. E. J., Mann, I. R., Rae, I. J., Sibeck, D. G., Boyd, A. J., et al. (2018). The global statistical response of the outer radiation belt during geomagnetic storms. *Geophysical Research Letters*, *45*(9), 3783–3792. https://doi.org/10.1002/2017GL076674

Nishimura, Y., Artemyev, A. V., Lyons, L. R., Gabrielse, C., Donovan, E. F., & Angelopoulos, V. (2022). Space-ground observations of dynamics of substorm onset beads. *Journal of Geophysical Research: Space Physics*, *127*(2), e2021JA030004. https://doi.org/10.1029/2021JA030004

Nishimura, Y., Yang, J., Pritchett, P. L., Coroniti, F. V., Donovan, E. F., Lyons, L. R., et al. (2016). Statistical properties of substorm auroral onset beads/rays. *Journal of Geophysical Research: Space Physics*, *121*(9), 8661–8676. https://doi.org/10.1002/2016JA022801

Oberhagemann, L. R., & Mann, I. R. (2020). A new substorm onset mechanism: Increasingly parallel pressure anisotropic ballooning. *Geophysical Research Letters*, *47*(2), e2019GL085271. https://doi.org/10.1029/2019GL085271

Ohtani, S., Miyashita, Y., Singer, H., & Mukai, T. (2009). Tailward flows with positive B_Z in the near-Earth plasma sheet. *Journal of Geophysical Research*, *114*(A6), A06218. https://doi.org/10.1029/2009JA014159

Panov, E. V., Lu, S., & Pritchett, P. L. (2020). Understanding spacecraft trajectories through detached magnetotail interchange heads. *Journal of Geophysical Research: Space Physics*, *125*(5), e2020JA027930. https://doi.org/10.1029/2020JA027930

Panov, E. V., Lu, S., & Pritchett, P. L. (2022). Magnetotail ion structuring by kinetic ballooning-interchange instability. *Geophysical Research Letters*, *49*(3), e2021GL096796. https://doi.org/10.1029/2021GL096796

Panov, E. V., Nakamura, R., Baumjohann, W., Sergeev, V. A., Petrukovich, A. A., Angelopoulos, V., et al. (2010). Plasma sheet thickness during a bursty bulk flow reversal. *Journal of Geophysical Research*, *115*(A5), A05213. https://doi.org/10.1029/2009JA014743

Panov, E. V., Sergeev, V. A., Pritchett, P. L., Coroniti, F. V., Nakamura, R., Baumjohann, W., et al. (2012). Observations of kinetic ballooning/interchange instability signatures in the magnetotail. *Geophysical Research Letters*, *39*(8), L08110. https://doi.org/10.1029/2012GL051668

Perraut, S., Contel, O. L., Roux, A., & Pedersen, A. (2000). Current-driven electromagnetic ion cyclotron instability at substorm onset. *Journal of Geophysical Research*, *105*(A9), 21097–21107. https://doi.org/10.1029/2000JA900059

Rae, I. J., Mann, I. R., Angelopoulos, V., Murphy, K. R., Milling, D. K., Kale, A., et al. (2009). Near-Earth initiation of a terrestrial substorm. *Journal of Geophysical Research*, *114*(A7), A07220. https://doi.org/10.1029/2008JA013771

Rae, I. J., Mann, J. R., Murphy, I. R., Milling, K. R., Parent, D. K., Angelopoulos, A., et al. (2009). Timing and localization of ionospheric signatures associated with substorm expansion phase onset timing and localization of ionospheric signatures associated with substorm expansion phase onset timing and localization of ionospheric signatures associated. *Journal of Geophysical Research*, *114*, A00C09. https://doi.org/10.1029/2008JA013559

Rae, I. J., Murphy, K. R., Watt, C. E. J., & Mann, I. R. (2011). On the nature of ULF wave power during nightside auroral activations and substorms: 2. Temporal evolution. *Journal of Geophysical Research*, *116*(A5), A00I22. https://doi.org/10.1029/2010JA015762

Rae, I. J., Murphy, K. R., Watt, C. E. J., Mann, I. R., Yao, Z., Kalmoni, N. M. E., et al. (2017). Using ultra-low frequency waves and their characteristics to diagnose key physics of substorm onset. *Geoscience Letters*, *4*(1), 23. https://doi.org/10.1186/s40562-017-0089-0

Rae, I. J., Watt, C. E. J., Mann, I. R., Murphy, K. R., Samson, J. C., Kabin, K., & Angelopoulos, V. (2010). Optical characterization of the growth and spatial structure of a substorm onset arc. *Journal of Geophysical Research*, *115*(A10), A10222. https://doi.org/10.1029/2010JA015376

Rae, I. J., Watt, C. E. J., Murphy, K. R., Frey, H. U., Ozeke, L. G., Milling, D. K., & Mann, I. R. (2012). The correlation of ULF waves and auroral intensity before, during and after substorm expansion phase onset. *Journal of Geophysical Research*, *117*(A8), A08213. https://doi.org/10.1029/2012JA017534

Ream, J. B., Walker, R. J., Ashour-Abdalla, M., El-Alaoui, M., Wiltberger, M., Kivelson, M. G., & Goldstein, M. L. (2015). Propagation of Pi2 pulsations through the braking region in global MHD simulations. *Journal of Geophysical Research: Space Physics*, *120*, 10574–10591. https://doi.org/10.1002/2015JA021572

Runov, A., Angelopoulos, V., Artemyev, A., Weygand, J., Lu, S., Lin, Y., & Zhang, X.-J. (2021). Global and local processes of thin current sheet formation during substorm growth phase. *Journal of Atmospheric and Solar-Terrestrial Physics*, *220*, 105671. https://doi.org/10.1016/J.JASTP.2021.105671

Runov, A., Angelopoulos, V., Sitnov, M. I., Sergeev, V. A., Bonnell, J., McFadden, J. P., et al. (2009). THEMIS observations of an earthward-propagating dipolarization front. *Geophysical Research Letters*, *36*(14), L14106. https://doi.org/10.1029/2009GL038980

Runov, A., Angelopoulos, V., Zhou, X.-Z., Voronkov, I. O., Kubyshkina, M. V., Nakamura, R., et al. (2008). Multipoint in situ and ground-based observations during auroral intensifications. *Journal of Geophysical Research*, *113*(A1), A00C07. https://doi.org/10.1029/2008JA013493

Sakaguchi, K., Shiokawa, K., Ieda, A., Nomura, R., Nakajima, A., Greffen, M., et al. (2009). Fine structures and dynamics in auroral initial brightening at substorm onsets. *Annales Geophysicae*, *27*(2), 623–630. https://doi.org/10.5194/angeo-27-623-2009

Schmid, D., Nakamura, R., Volwerk, M., Plaschke, F., Narita, Y., Baumjohann, W., et al. (2016). A comparative study of dipolarization fronts at MMS and Cluster. *Geophysical Research Letters*, *43*(12), 6012–6019. https://doi.org/10.1002/2016GL069520

Sergeev, V. A., Angelopoulos, V., & Nakamura, R. (2012). Recent advances in understanding substorm dynamics. *Geophysical Research Letters*, *39*(5), L05101. https://doi.org/10.1029/2012GL050859

Sergeev, V. A., Apatenkov, S. V., Angelopoulos, V., McFadden, J. P., Larson, D., Bonnell, J. W., et al. (2008). Simultaneous THEMIS observations in the near-tail portion of the inner and outer plasma sheet flux tubes at substorm onset. *Journal of Geophysical Research*, *113*(A1), A00C02. https://doi.org/10.1029/2008JA013527

Slavin, J. A., Baker, D. N., Craven, J. D., Elphic, R. C., Fairfield, D. H., Frank, L. A., et al. (1989). CDAW 8 observations of plasmoid signatures in the geomagnetic tail: An assessment. *Journal of Geophysical Research*, *94*(A11), 15153. https://doi.org/10.1029/JA094iA11p15153

Slavin, J. A., Owen, C. J., Kuznetsova, M. M., & Hesse, M. (1995). ISEE 3 observations of plasmoids with flux rope magnetic topologies. *Geophysical Research Letters*, *22*(15), 2061–2064. https://doi.org/10.1029/95GL01977

Smith, A. W., Rae, I. J., Forsyth, C., Watt, C. E., Murphy, K. R., & Mann, I. R. (2020). Diagnosing the time-dependent nature of magnetosphere-ionosphere coupling via ULF waves at substorm onset. *Journal of Geophysical Research: Space Physics*, *125*(11), e2020JA028573. https://doi.org/10.1029/2020JA028573

Smith, A. W., Rae, I. J., Forsyth, C., Watt, C. E. J., & Murphy, K. R. (2020). On the magnetospheric ULF wave counterpart of substorm onset. *Journal of Geophysical Research: Space Physics*, *125*(4), e2019JA027573. https://doi.org/10.1029/2019JA027573

Snekvik, K., Tanskanen, E., Østgaard, N., Juusola, L., Laundal, K., Gordeev, E. I., & Borg, A. L. (2012). Changes in the magnetotail configuration before near-Earth reconnection. *Journal of Geophysical Research*, *117*(A2), A02219. https://doi.org/10.1029/2011JA017040

Stix, T. H. (1992). *Waves in plasmas*. American Institute of Physics. Retrieved from https://www.springer.com/gp/book/9780883188590

Sun, W. J., Fu, S. Y., Wei, Y., Yao, Z. H., Rong, Z. J., Zhou, X. Z., et al. (2017). Plasma sheet pressure variations in the near Earth magnetotail during substorm growth phase: THEMIS observations. *Journal of Geophysical Research: Space Physics*, *122*(12), 12212–12228. https://doi.org/10.1002/2017JA024603

Uritsky, V. M., Liang, J., Donovan, E., Spanswick, E., Knudsen, D., Liu, W., et al. (2009). Longitudinally propagating arc wave in the pre-onset optical aurora. *Geophysical Research Letters*, *36*(21), L21103. https://doi.org/10.1029/2009GL040777

Viñas, A. F., & Madden, T. R. (1986). Shear flow-ballooning instability as a possible mechanism for hydromagnetic fluctuations. *Journal of Geophysical Research*, *91*(A2), 1519. https://doi.org/10.1029/JA091iA02p01519

Virtanen, P., Gommers, R., Oliphant, T. E., Haberland, M., Reddy, T., Cournapeau, D., et al. (2020). SciPy 1.0: Fundamental algorithms for scientific computing in python. *Nature Methods*, *17*(3), 261–272. https://doi.org/10.1038/s41592-019-0686-2

Voronkov, I., Donovan, E. F., & Samson, J. C. (2003). Observations of the phases of the substorm. *Journal of Geophysical Research*, *108*(A2), 1073. https://doi.org/10.1029/2002JA009314

Voronkov, I., Rankin, R., Frycz, P., Tikhonchuk, V. T., & Samson, J. C. (1997). Coupling of shear flow and pressure gradient instabilities. *Journal of Geophysical Research*, *102*(A5), 9639–9650. https://doi.org/10.1029/97JA00386

Walach, M., & Grocott, A. (2019). SuperDARN observations during geomagnetic storms, geomagnetically active times, and enhanced solar wind driving. *Journal of Geophysical Research: Space Physics*, *124*(7), 5828–5847. https://doi.org/10.1029/2019JA026816

Walsh, A. P., Owen, C. J., Fazakerley, A. N., Forsyth, C., & Dandouras, I. (2011). Average magnetotail electron and proton pitch angle distributions from Cluster PEACE and CIS observations. *Geophysical Research Letters*, *38*(6), L06103. https://doi.org/10.1029/2011GL046770

Walt, S. V. D., Colbert, S. C., & Varoquaux, G. (2011). The NumPy array: A structure for efficient numerical computation. *Computing in Science & Engineering*, *13*(2), 22–30. https://doi.org/10.1109/MCSE.2011.37

Wang, C.-P., Lyons, L. R., Nagai, T., & Samson, J. C. (2004). Midnight radial profiles of the quiet and growth-phase plasma sheet: The Geotail observations. *Journal of Geophysical Research*, *109*(A12), A12201. https://doi.org/10.1029/2004JA010590

Yue, C., Wang, C., Nishimura, Y., Murphy, K. R., Xing, X., Lyons, L., et al. (2015). Empirical modeling of 3-D force-balanced plasma and magnetic field structures during substorm growth phase. *Journal of Geophysical Research: Space Physics*, *120*(8), 6496–6513. https://doi.org/10.1002/2015JA021226

Zhu, P., Bhattacharjee, A., & Ma, Z. W. (2004). Finite k_y ballooning instability in the near-Earth magnetotail. *Journal of Geophysical Research*, *109*(A11), A11211. https://doi.org/10.1029/2004JA010505